Applied Materials Today 25 (2021) 101237

Contents lists available at ScienceDirect

Applied Materials Today

journal homepage: www.elsevier.com/locate/apmt

Magnetically propelled soft microrobot navigating through constricted microchannels

Jinrun Liu[a], Shimin Yu[b], Borui Xu[a], Ziao Tian[a], Hehua Zhang[a], Kaipeng Liu[b], Xiaojie Shi[a], Zhe Zhao[a], Chang Liu[a], Xinyi Lin[a], Gaoshan Huang[a], Alexander Aleksandrovic Solovev[a], Jizhai Cui[a,*], Tianlong Li[b,*], Yongfeng Mei[a]

[a] Department of Materials Science, State Key Laboratory of ASIC and Systems, Fudan University, 220 Handan Road, Shanghai, Shanghai 200433, People's Republic of China
[b] State Key Laboratory of Robotics and System, Harbin Institute of Technology, 92 West Dazhi Street, Harbin 150001, People's Republic of China

ARTICLE INFO

Article history:
Received 7 July 2021
Revised 10 October 2021
Accepted 19 October 2021
Available online 7 November 2021

Keywords:
Soft microrobot
Magnetic control
Micromanipulation
Adaptive motion

ABSTRACT

Recent strides in microfabrication technologies offer important possibilities for developing microscale robotic systems with enhanced power, functionality and versatility. Previous microrobots fabricated by lithographic techniques usually lack the ability to adaptively deform in confined and constricted spaces and navigate through, therefore hindering their applications in complex biological environments. Here, a microfluidic strategy is combined with a dip-coating process for continuous fabrication of soft helical structures with controllable mechanical property as magnetically propelled microrobots, capable of actively propelling through narrow and sinuous microchannels. Because of their self-adaptive deformation capability, the magnetically propelled soft microrobots can actively navigate through a narrow opening, 2.21 times smaller than the sectional area of the microrobot, and a U-shape-bent capillary, directed by a programmed magnetic field. Additionally, the soft microrobot demonstrates increased swimming speed in a fluid of high viscosity, because of the adaptive tightening deformation of the helix when swimming. This new magnetically propelled soft microrobot and its attractive performance will open up new possibilities for biomedical operation at the micro and nanoscale.

1. Introduction

Inspired by the nature-approved propulsion strategies of a myriad of biomolecules and living microorganisms, considerable efforts have been devoted to the development of micro-/nanorobots that can achieve effective propulsion at a low Reynolds number [1–6]. These microrobots that use different propulsion methods, involving local chemical fuel [7,8] or external electrical [9–13], optical [14–17], ultrasonic [18–22], and magnetic fields [23–28], are capable of performing self-propelled motions to overcome obstacles associated with viscous forces and Brownian motion. Among these developed methods for micro-/nanorobots locomotion, the use of magnetic fields has been popular due to remote navigation and non-invasive propulsion.

Magnetic microrobots are widely applied in biomedicine [29], sensing [30–32], environmental remediation [33], and nanofabrication [34–37]. Magnetic field can be safely applied to biological systems without obvious side effects [29]. The functionalized microrobots can navigate in biological entities which is hard to reach by other devices, such as intraperitoneal cavity [38,39], blood vessel [40,41] and even vitreous [25] for minimal invasive operation and targeted therapy [42]. In previous work, microrobots mainly operate in working environment much larger than their characteristic size, where they can swim freely with little or no obstables. In fact, many biological environment are narrow and sinuous (such as blood vessels), and in many cases (such as capillaries) smaller than the size of the robots; therefore the microrobots require an adaptive deformation strategy so that they can operate in these confined places. Few previously reported microrobots offer such capabilities, since they are generally made by rigid materials with limited deformability.

In nature, red blood cells (RBC) can adaptively deform and pass through narrow blood vessels with openings smaller than their original size [6]. Mimicking this natural deformability is essential for the development of microrobots, especially for biomedical applications. Huang et al. develoepd compliant soft microrobots that can *passively* pass through a constricted capillary along with an externally applied flow of fluids [41]. In this work, we present magnetically propelled soft microrobots that can *actively* swim through

* Corresponding authors.
E-mail addresses: jzcui@fudan.edu.cn (J. Cui), tianlongli@hit.edu.cn (T. Li).

https://doi.org/10.1016/j.apmt.2021.101237
2352-9407/

such narrow openings and sinuous microchannels. A soft material with tunable mechanical property is used to fabricate the soft helical microrobots. A low-cost coaxial capillary microfluidic systems combined with the dip-coating process are employed to fabricate the structure of the microrobots, which are composed of calcium alginate (Ca-Alg), poly(ethyleneglycol) diacrylate (PEGDA) hydrogel and γ-Fe_2O_3 nanoparticles. By adjusting the PEGDA percentage in the materials and the subsequently treatment Na^+/Ca^{2+} solutions, the elastic moduli of the materials are tunable from a few MPa down to tens of kPa. In response to a three degree of freedom uniform rotating magnetic field, these soft helical microrobots performed *E.Coli*-like corkscrew motion in low Reynolds number fluid. A maximum speed of 3247.42 μm/s was recorded for the reported soft helical microrobots (elastic modulus of the sample E = 1.35 MPa) at a driving frequency of 55 Hz and magnetic field strength of 25 mT, and lower magnetic fields induces a lower step-out frequency and slower motion. The detailed results and the swimming performance of the mcirorobots with different morphology parameters are shown in Fig. S1 and discussed in Fig. S2 in the Supporting Information, respectively.

Locomotion of these microrobots in constricted microchannels under programmed magnetic field was also demonstrated, and the microrobots could pass through the narrow opening 2.21 times smaller than their sectional area. Finite element analysis was implemented to study the process of passing through the narrow opening, which shows that for microrobots of the same size and geometry, the ones made by low modulus materials induce smaller friction force during the process. Only when the propulsion force is larger than the friction, the microrobot is able to pass through. Moreover, the soft microrobots were able to pass through bent capillaries. The soft microrobot with much lower elastic modulus (E = 0.069 MPa) demonstrated unique tightening behavior when swimming in viscous liquid, inducing increased swimming speed. These microrobots and their excellent performance in complex environments will open up new possibilities for biomedical operation at the nanoscale.

2. Materials and methods

2.1. Chemicals and reagents

Sodium Alginate (Na-Alg), radical photoinitiator 2- hydroxyl–2-methylpropiophenone (Darocure 1173) and γ-Fe_2O_3 magnetic nanoparticle (10 nm) were purchased from Aladdin Industrial Corporation (USA), poly(ethyleneglycol) diacrylate (PEGDA, Average Mn = 700), phosphate buffered saline (PBS pH 7.2), and octadecyltrimethoxysilane were purchased from Sigma Aldrich Corporation (USA), sodium chloride (NaCl), calcium chloride ($CaCl_2$) and poly (vinyl alcohol) (PVA, Mw 13,000~23,000) were provided by Hushi Corporation (China). Capillaries were provided by Jinglai Corporation (China). Microscope slides were purchased from Sail Brand (China). Epoxy adhesive were purchased from Ailete (China). Gelatin was purchased from Zhanyi Corporation (China).

The composed materials of the soft microrobot are all biocompatible and biodegradable. Alginate is extracted from brown algae and reported to degrade in the present of amylase (a human enzyme) [43]. For poly (ethylene glycol) diacrylate (PEGDA), it can be degraded by the hydrolytic cleavage of the ester bonds [44], and the products are poly (ethylene glycol) (PEG) and poly (acrylic acid) (PAA), with no harm and widely used in biomedical applications [45]. Fe_2O_3 nanoparticles is also biocompatible, and has been approved for the treatment of iron deficiency anemia by FDA [46].

2.2. Fabrication of the coaxial capillary microfluidic system

The tapered injection cylindrical capillaries were prepared by a capillary fuse stretcher (PC-10, NARISHIGE, Japan), and sand paper was used to polish the tips to 50–90 μm. The obtained capillaries were treated with octadecyltrimethoxysilane to be hydrophobic. The collection capillary's inner diameter decides the diameter of the synthesized helical structure. In this work, we used ~220 μm capillaries as received. The injection and collection capillaries were aligned in the center of a square capillary and fixed with five-minute epoxy adhesive. It is worth noting that smaller microrobots can be fabricated by smaller collection capillaries and injection capillary tips.

2.3. Preparation and characterization of solutions

Outer phase (2 wt% $CaCl_2$ in 5 wt% PVA aqueous) was prepared by mixing 2.0 g $CaCl_2$ in 100 mL 5% PVA aqueous, followed by stirring the solutions for 30 min. Inner phase (2 wt% Na-Alg, 20 wt% PEGDA hydrogel precursor) were prepared by mixing 0.95 g Na-Alg, 9.50 g PEGDA, 0.08 g Darocure 1173, and 35.00 mL H_2O together, followed by stirring for 120 min in the dark. Dip-coating magnetic nanoparticles slurry was prepared by dispersing 0.1 g magnetic γ-Fe_2O_3 nanoparticles in 50 mL DI water, followed by ultrasonic treatment for 6 h. The measurement of the viscosity of the solution with varying concentration of PVA was conducted by a rotary rheometer (HAAKE MARSIII, Thermo-Fisher, USA), see detail in Fig. S3 in Supporting Information. The clogged area in the capillary is prepared by 5 wt% gelatin and red-dyed deionized water. Rheological measurement (oscillation) of the gelatin was performed by a rotary rheometer at OSC mode at 24 °C and 2 Hz.

2.4. Fabrication of soft microrobots

The inner phase and the outer phase were injected by a microfluid pump (PHD ULTRA, Harvard, USA) in appropriate rates. When the inner phase is injected into outer phase, a cross-linked water-insoluble Ca-Alg hydrogel template will be formed as Ca^{2+} diffuses into inner phase hydrogel precursor. By adjusting the flow rate ratio of inner phase and outer phase, various shapes of Ca-Alg will be formed, from straight to sinusoidal, helical, respectively, and the helical patch can be controlled, too [47]. During the forming of Ca-Alg template, it is exposed to UV light to make the PEGDA be polymerized. For dip-coating process, the collected samples were incubated in the as-prepared magnetic slurry for 1 h with mild shaking to coat γ-Fe_2O_3 magnetic nanoparticles. After being rinsed in DI water for several times, they were cut into desired lengths by blades. The yield in terms of number of microrobots for 1 mL hydrogel precursor was calculated more than tens of thousands.

2.5. Characterization of soft microrobots

Optical microscopy images of the samples were obtained by an optical microscope (BX51TRF, Olympus Corporation, Japan). To characterize the mechanical properties of the samples, the moduli of elasticity in tension of the samples containing different PEGDA amounts (0, 10, 20, 30 wt%) and the post-treated samples were tested by an electronic universal material testing machine (Tensile testing system 5966, Instron Limited, UK). The samples for the FE-SEM (by a scanning electronic microscope Nova NanoSEM 450, FEI corporation, USA), elemental mapping (by a EDX spectroscopy X-Max^N 50mm^2, Oxford Instruments, UK), FTIR test (Nicolet 6700, ThermoFisher, USA) and magnetic properties test (by a vibrating sample magnetometer MPMS (SQUID) VSM, Quantum Design Cor-

poration, USA) were pretreated by super critical drying process by a critical point dryer (CPD030, Leica, Germany).

2.6. 3D Helmholtz coils setup

The 3D Helmholtz coils setup was demonstrated in detail in our previous work [48–50]. The mechanism is based on electromagnetic effect. The alternating signal was programmed by computer and generated by a high-speed voltage output device. And an amplifier is used to amplify the current and activate the Helmholtz coils. Three pairs of orthogonal Helmholtz coils were used to generate uniform rotating magnetic field with intensity from 0 to 25 mT under frequency of 200 Hz. The setup was integrated on an inverted microscope (iX73P1F, Olympus, Japan), and the sample holder was placed in the center of Helmholtz coil setup to avoid the magnetic inhomogeneity. A rotating magnetic field was applied to provide the mechanical torque that propels the soft magnetic microrobots, and videos were recorded using a high-speed camera (FR-180, Norpix Inc., Canada). The optical image of the setup is shown in Fig. S4 in the Supporting Information.

2.7. Fabrication of sinuous microchannels

The microchannels were capillaries (diameter~300 μm) which were shaped into different configurations by a capillary fuse stretcher. The capillaries were firstly sonicated in deionized water and ethanol for one minute for four times, and then heated by the capillary fuse stretcher to 65 °C to soften the capillary. In this temperature, the capillaries were processed into different shapes by a micromanipulator. Lastly, the processed capillaries were cooled down to room temperature.

3. Results and discussion

Mimicking the naturalistic deformability of RBC to pass through narrow and sinuous microvessels is essential for the development of microrobots, especially in biomedical applications. In order obtain such deformability, a microfluidic strategy combined with a dip-coating process is employed to fabricate the soft microrobots. Microfluidics technique can manipulate fluids in small dimensions, featuring continuous synthesis of soft materials in varieties of morphologies. Integrating biocompatible hydrogel with microrobots is of great significance because hydrogels' physico-chemical and mechanical properties are similar to those of creatures [51]. As displayed schematically in Fig. 1a, a coaxial capillary microfluidic system was employed to fabricate the desired helical soft microrobots. The soft microrobots are composed of three biocompatible materials. Among them, Sodium Alginate (Na-Alg) is a natural anionic polysaccharide extracted from brown algae. Poly(ethylene glycol) diacrylate (PEGDA) is also of high mechanical stability due to the formation of double bonds after UV-irradiation [52]. γ-Fe_2O_3 magnetic nanoparticle is a FDA-approved inorganic material that are suitable for clinical use. All of these materials are biocompatible and widely investigated in biomedical applications. Fig. S5a shows the microfluidic device, and Fig. S5b shows a microscopic image of the microstructure in the microfluidic device during formation of the hydrogel helix in the Supporting Information. The fabrication process of helical microrobot can be divided into two steps. First, due to the immediate gelation and unbalanced fluidic friction between the gelated microfiber and surrounding fluid, the spiraled microfiber occurred in the inner tubular capillary, when the Ca-Alg and PEGDA mixed liquid flow was injected into a calcium chloride solution. Then the semi-gelated microfiber was exposed to ultraviolet irradiation, and double bonds among PEGDA molecules were formed. The as-prepared Ca-Alg/PEGDA microfiber is in helical shape (see Fig. S6a in the Supporting Information). Second, the dip-coating process was used to render the helical microstructure magnetic, by incubating them in γ-Fe_2O_3 nanoparticles slurry for 1 h accompanied with mild shaking, followed by cutting into desired lengths (see Fig. S6b in the Supporting Information). The morphology of the original Ca-Alg helical structure kept intact after dip-coating (see Fig. S6d and S6f). The γ-Fe_2O_3 nanoparticles were uniformly and firmly distributed on Ca-Alg/PEGDA helical structure, which can withstand sonification treatment (see Fig. S6j) [29]. The morphology of the original Ca-Alg/PEGDA helical structure kept intact after dip-coating, and the γ-Fe_2O_3 nanoparticles were uniformly distributed on Ca-Alg/PEGDA helical structure. The magnetic particles amount is comparable to previously reported study, and the magnetic materials loaded on helical microswimmers reported in recent years were summarized in Table S1 in the Supporting Information. The samples' Fourier transform infrared spectroscopy (FTIR) results, SEM images, their corresponding elemental mapping, the magnetic hysteresis loops, and EDXS analysis results were all characterized in Fig. S6.

During the fabrication process, the ratio of the inner flow rate to the outer flow rate is critical to the shape of semi-gelated microfiber. When the outer calcium chloride flow rate was sufficiently larger than the inner Ca-Alg/PEGDA flow, microfiber shape was formed straight in the center of the collection tubular capillary induced by the hydrodynamic focusing effect, as shown in Fig. 1b-I. However, as the ratio of the inner flow rate to the outer flow rate increased, a sinusoidal structure formed in a two-dimensional plane (see Fig. 1b-II). In particular, as the inner to outer flow ratio increased to a certain threshold, due to the elastic energy accumulated by velocity difference between inner phase and outer phase, a rotary fluid field was formed in the collection capillary, thus generating a continuum helical structure (see Video S1 in the Supporting Information) with random chirality. The outer diameter of the helical structure was equal to or slightly smaller than the inner diameter of the collection tubular capillary, and the diameter of the microfiber was around the inner diameter of the injection capillary tip, so the size can be controlled by adjusting the diameters of the inner diameters of the collection capillary and the injection tip. By adjusting the flow rate ratio of inner phase and outer phase, pitch lengths of helical structure could be precisely controlled (see Fig. 1b II–IV) as well. When the inner to outer flow rate ratio was under certain rates, the capillaries would be blocked (see Fig. 1b-VI). All the inner and outer flow rates and their corresponding microstructure shapes during the fabrication process are summarized in Fig. 1c.

Based on this microfluidic fabrication strategy, the elastic modulus of the hydrogel of the microrobot can be readily adjusted. In nature, microorganisms adopt alternate-shaped flexible flagellar to optimize their motility in low *Re* number fluids. For example, taking advantage of a flagellar buckling instability, uniflagellated bacterium *Caulobacter crescentus* can perform two distinct modes of the motility [53]. The soft microrobot with lower modulus can deform in the presence of flow, indicating a promising polymorphic transformation when swimming in viscous liquids [54]. In this work, the PEDGA polymerized in semigelation microfiber template. The rendered covalent-crosslinked hydrogel matrix makes the helical structure mechanically stable, and the moduli after curing depends on the concentration of PEGDA in precursor. By immersing the microrobot into a certain mixing ratio of NaCl and $CaCl_2$ aqueous Na^+/Ca^{2+} solution I [$c(Na^+)$= 47.6 mg•mL^{-1}, $c(Ca^{2+})$= 0.952 mg•mL^{-1}] and Na^+/Ca^{2+} solution II [$c(Na^+)$= 49.0 mg•mL^{-1}, $c(Ca^{2+})$= 0.392 mg•mL^{-1}], the moduli can be further lowered. This is because monovalent cation (Na^+) can replace multivalent cation Ca^{2+} crosslinked in Ca-Alg when the gel is exposed to monovalent cation solution. This so-called gel-sol transformation decreases crosslinking density, thus reducing the elastic modulus [55]. To characterize the mechanical

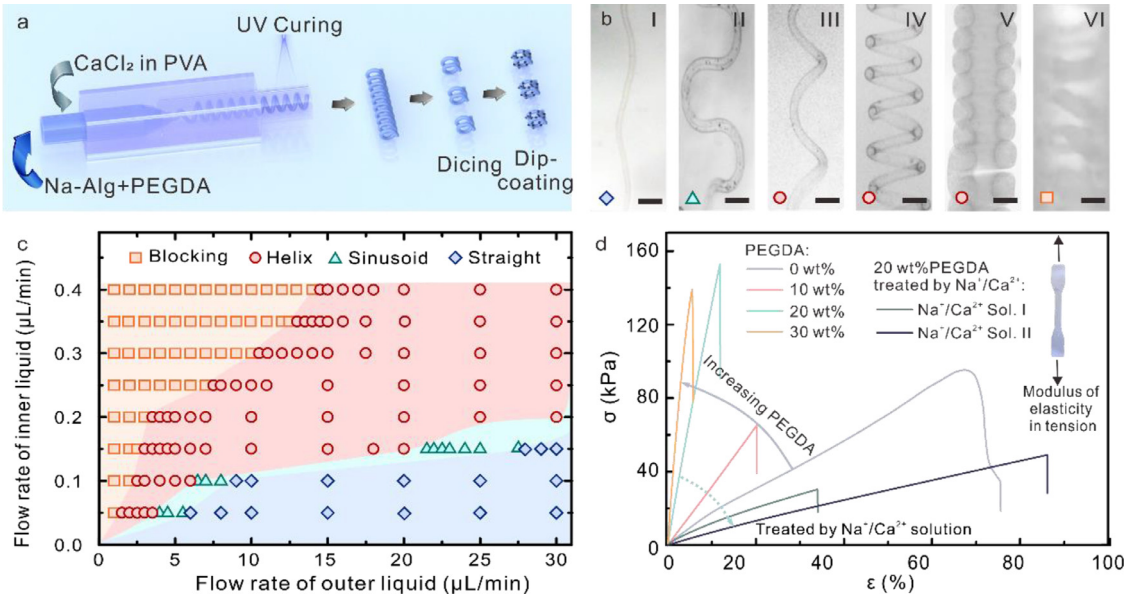

Fig. 1. Fabrication process, mophology and elastic properties of the soft microrobots. (a) Schematic of synthesis process of hydrogel microhelices. (b) Optical microscopic images of different hydrogel microfiber shapes controlled by inner to outer flow rate ratio: (I) straight hydrogel microfiber. (II) sinusoidal hydrogel microfiber. _(III–V) helical hydrogel microfiber with precisely controllable pitch. (VI) capillaries blocked. Scale bar, 100 μm. (c) Fabricated microfiber shapes against flow rate of inner and outer liquid. (d) Stress-Strain curves of various fabricated samples. The elastic moduli for the materials containing various concentrations (0, 10, 20, 30 wt%) of PEGDA are 0.17 MPa, 0.32 MPa, 1.35 MPa and 3.15 MPa, respectively. The elastic moduli of the 20 wt% PEGDA samples treated by Na^+/Ca^{2+} Sol. I [$c(Na^+)$= 47.6 mg•mL^{-1}, $c(Ca^{2+})$= 0.952 mg•mL^{-1}] and Na^+/Ca^{2+} Sol. II [$c(Na^+)$= 49.0 mg•mL^{-1}, $c(Ca^{2+})$= 0.392 mg•mL^{-1}] are 0.137 MPa, 0.069 MPa, respectively.

properties of the sample, the moduli of elasticity in tension of the samples containing different PEGDA concentrations (0, 10, 20 and 30 wt%) and the samples treated by Na^+/Ca^{2+} Sol. I and Na^+/Ca^{2+} Sol. II were tested and the results are shown in Fig. 1d. The elastic moduli of hydrogel samples are 0.17, 0.32, 1.35, 3.15 MPa (different PEGDA concentrations) and 0.137, 0.069 MPa (different Na^+/Ca^{2+} solutions), respectively, which are much lower than the modulus of SU-8 (E = 2000 MPa) photoresist, commonly used in previous rigid microrobots fabricated by photolithography method [56] or direct laser writing technology [57]. The morphology changed slightly when immersed in Na^+/Ca^{2+} Solutions, and the optical microscopy images were shown in Fig. S7.

Like RBCs in sinuous microvessels, these soft microrobots are capable of locomotion in sinuous environments due to the ability of adaptive deformation. The locomotion capability of the soft microrobots was demonstrated first in the presence of an sinusoidal bent capillary (Fig. 2a). The soft microrobot propelled under a uniform rotating magnetic field are used to demonstrate the concept. When the rotating direction of the external magnetic field changed, the microrobots can instantly align their magnetized axis to the magnetic field. The soft microrobot showed corkscrew motion (Fig. 2b-I-IV, Video S2) when passing through the sinuous microchannel. Here the direction of the rotating magnetic field is constant (Fig. 2b-II-IV), and the microrobot can adjust its swimming direction according to the direction of the microchannels, demonstrating adaptive motion due to its soft nature. The locomotion capability of the soft microrobots was also demonstrated in the presence of an orthometric bent capillary with an angle of 90 ° (Fig. 2c). At first the magnetic soft microrobot performed a typical corkscrew motion during approaching the bending part (Fig. 2d-I). When starting to contact the inner wall of the bending part (Fig. 2d-II), the head would be bent and perform a corkscrew motion under the programmed rotating magnetic field. As the programmed signal output continued to change, more part of the magnetic soft microrobot would align their magnetized axis to the magnetic field, steering the microrobot forward(Fig. 2d-III). After crossing the orthogonal part, the magnetic soft microrobot recovered its original shape and performed corkscrew motion as before (Fig. 2d-IV, Video S3). In addition, the direction magnetic field can also be continuously adjusted to pass through various complex microchannels, for example, passing through the 180° 'U' shape bent capillary, as shown schematically and experimentally in Fig. 2e,f, and Video S4. Living systems contain flowing fluids rather than static ones, the ability to swim upstream against in biological fluids ensure the potential applications *in vivo*. In order to study whether the soft microrobot can produce propulsion power in practice, we directed it against an artificial biological fluid (Phosphate buffer saline dispersed with PS microsphere) flowing stream, see detail in Fig. S8. The microrobot generated sufficient propulsion speed to upstream against flow, indicating that the soft microrobot has potential to operate against flow in biological environments.

Further, microrobots made by soft hydrogels with low moduli are shown to pass through narrow openings inspired by soft RBC passing through microvessels with a sectional area even smaller than their cell size (Fig. 2g). To investigate the motion behavior of soft microrobots, a subuliform capillary, with minimal inner sectional area of 1.4 × 10^4 μm^2, was employed to mimic the narrow opening of blood vessels. Fig. 2h and corresponding Video S5 in the Supporting Information show the resulting continuous motion of soft microrobots by applying an external magnetic field with a frequency of 5 Hz in the subuliform capillary. The diameter of the microrobot is 200 μm and the sectional area is 3.1 × 10^4 μm^2 which is 2.21 times larger than the minimal inner sectional area of the subuliform capillary. The magnetic propelled soft microrobot performed a typical corkscrew motion when approaching the narrow openings. When the microrobot started to contact with the narrow opening, the microrobot bent the body for decreasing the sectional area to pass through the narrow opening. After crossing the narrow opening, the soft microrobot recovered to the original shape. Here the torso diameter (*i. e.*, 2r in Fig. S1-a) of the microrobot is 99.2 μm. We've also prepared microrobots with different torso diameters. While smaller torso is structrally softer with better deformability, magnetic nanoparticles loading amount on smaller torso is inevitably decreased due to a smaller surface area.

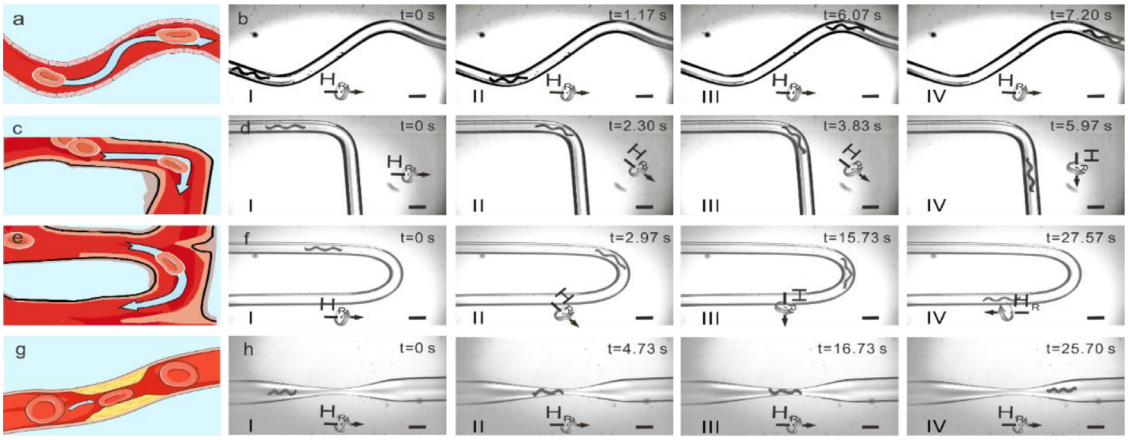

Fig. 2. (a) Schematic illustration of magnetic soft microrobot's adaptive motion to pass through a sinuous capillary, inspired by RBC passing through winding microvessels. (b) Time lapse images of magnetic soft microrobot's adaptive motion to pass through the sinuous capillary. Scale bar, 200 μm (c) Schematic illustration of magnetic soft microrobot's adaptive motion to pass through an orthometric bent capillary, inspired by RBC passing through orthometric microvessels. (d) Time lapse images of magnetic soft microrobot's adaptive motion to pass through the orthometric bent capillary. Scale bar, 200 μm. (e) Schematic illustration of magnetic soft microrobot's adaptive motion to pass through a 'U' shape bent capillary, inspired by a red blood cell passing through 'U' shape microvessels. (f) Time lapse images of magnetic soft microrobot's adaptive motion to pass through the U' shape bent capillary. Scale bar, 200 μm. (g) Schematic illustration of magnetic soft microrobot's adaptive motion to pass through a subuliform capillary, inspired by RBCs passing through narrow microvessel openings. (h) Time lapse images of magnetically propelled soft microrobot's adaptive deformative motion to pass through a subuliform capillary. Scale bar, 500 μm.

In view of balancing magnetic propulsion force and deformability, an optimized diameter of 90–100 μm is adopted in this work. The microrobot can also be used to penetrate and clear clots in the microvessels, showing the potential of removing blood clots in biological circulatory system, see detail in Fig. S9 and Video S6. We also performed preliminary drug release test using methylene blue as model drug, see detail in Fig. S10. And from perspective of applications, our microrobot can be imaged and tracked based on different medical imaging methods, such as ultrasound imaging [58], positron emission tomography [59], and magnetic resonance imaging [60].

We perform finite element simulation to study the stress distribution of the soft microrobot when passing through the subuliform tube, as shown in Fig. 3a. Induced by the adaptive deformation of soft microrobots, the stress concentration region are on the surface of microrobot in contact with the wall of the subuliform capillary. The real-time velocity was shown in Fig. 3b. It can be seen that the velocity fluctuated around 290 μm/s before contacting with the subuliform surface. As the microrobot touched the wall, the contacting force increased markedly, and the velocity decreased to 20 micrometers per second. The reason is that the energy loss to offset the contacting resistance in the advance process. When it went out, the contacting force declined rapidly, and the velocity responds rapidly to the contacting force change, reverting to the initial value (~290 μm/s). The soft feature of the material is critical for the microrobot's adaptive deformation and passing through the subuliform tube. Such elastic deformation induces contact force on the microrobot against the wall of the subuliform tube and friction forces impeding the passing through process. Finite element method was used to analyze the contact pressure of the microrobot when compressed by the wall and the results are shown in Fig. S11 and Table S2 in the Supporting Information. Multiplying the contact forces with the friction coefficient (assumed to be 0.007) [61], we can get the calculated friction forces for hydrogels in six different moduli used in this work, as shown in Fig. 3c. It's indicated that for when passing through a specific narrow opening, the microrobot in high modulus induces high friction force (up to 8.8 $\times$ 10^{-8} N for hydrogels with 3.15 MPa elastic modulus), while microrobot in low modulus induces much lower friction force (0.2 $\times$ 10^{-8} N for hydrogels with 0.069 MPa elastic modulus).

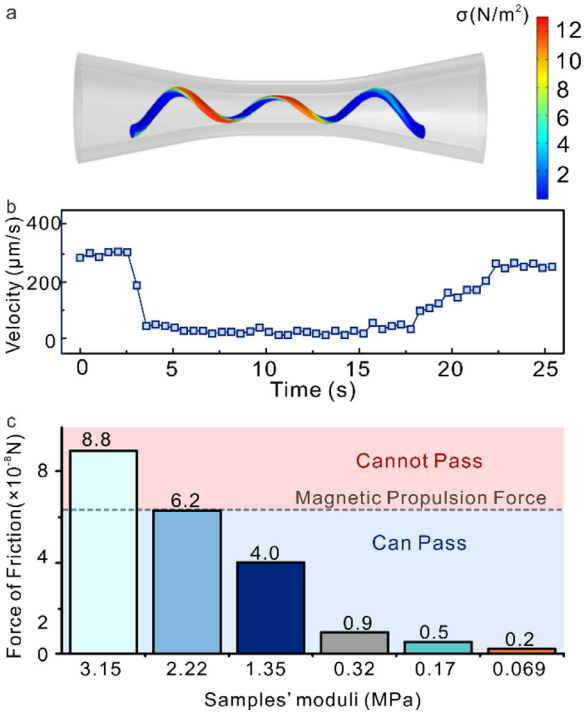

Fig. 3. (a) Simulations showing the stress distribution of microrobots for crossing the subuliform capillary via a uniform rotating magnetic field. (b) Real-time velocity of microrobots during the adaptive deformative motion to pass through a subuliform capillary. (c) The calculated frictional force of samples in different moduli.

The microrobot can pass through the subuliform narrow opening only when the magnetic propulsion force is larger than the friction. Resistive force theory [2] is used to calculate the propulsion force of the microrobot during the corkscrew motion (Eq. (1)).

$$\begin{pmatrix} F \\ T \end{pmatrix} = \begin{pmatrix} a & b \\ b & c \end{pmatrix} \begin{pmatrix} v \\ \omega \end{pmatrix} \tag{1}$$

where the F is the applied force, T is the applied torque, v is the forward velocity, ω is the angular velocity, and the coefficients a, b,

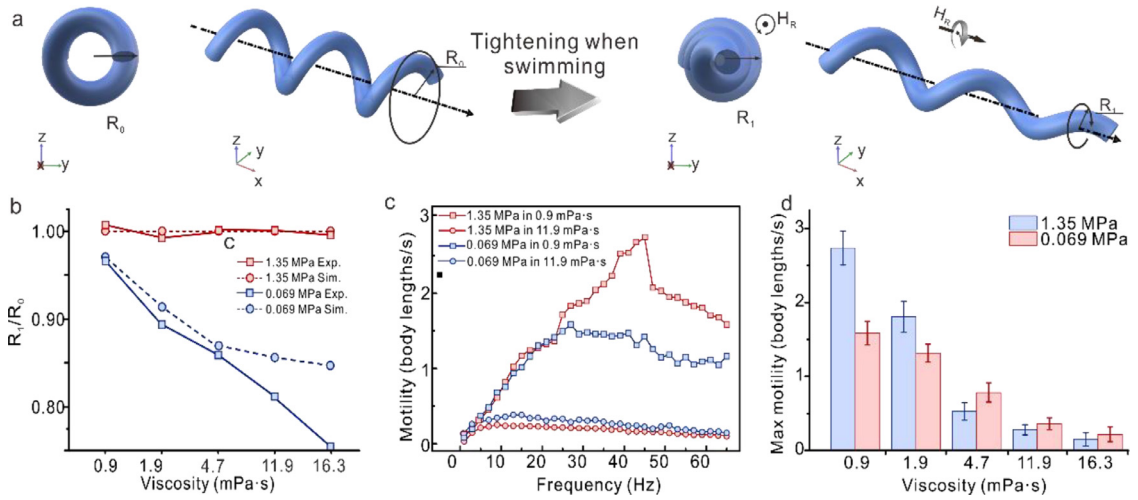

Fig. 4. (a) Schematic illustration of soft microrobot's tightening deformation when swimming. (b) Radius change of soft microrobots of different modulus in serial viscosity solutions, in modeling and experiments results. (c) Dependence of microrobots motility of different modulus samples on rotation frequency in different viscosity fluids. (d) Max motility of different modulus soft microrobots in serial viscosity fluids.

and c which are modeled with resistive force theory can be shown as follows (see Eqs. (2)–(4)):

$$a = 2\pi nR\left(\frac{\xi_{//}\cos^2\alpha + \xi_n\sin^2\alpha}{\sin\alpha}\right) \tag{2}$$

$$b = 2\pi nR^2\xi_{//} - \xi_n\cos\alpha \tag{3}$$

$$c = 2\pi nR^3\left(\frac{\xi_{//}\sin^2\alpha + \xi_n\cos^2\alpha}{\sin\alpha}\right) \tag{4}$$

where R is the radius of the helical structure, α is the helix angle, n is the number of the minimum period shape.

Lighthill's resistive force coefficients along ($\xi_{\parallel}$) and perpendicular (ξ_n) to the helix axis for calculation result in Eqs. (5)–(7) [62]:

$$\xi_{//} = \frac{2\pi\eta}{\ln(2q/r) - 0.5} \tag{5}$$

$$\xi_n = \frac{4\pi\eta}{\ln(2q/r) + 0.5} \tag{6}$$

$$q = 0.09\lambda \tag{7}$$

In our experimental case, the sample measures $2R = 254.0\ \mu$m, so the maximum force $F = 6.2 \times 10^{-8}$ N, the maximum torque is $T = 3.29 \times 10^{-13}$ N•m. For the microrobots made by the six types of materials fabricated in this work, the hydrogels with 0 wt%, 10 wt% PEGDA and 20 wt% PEGDA treated by Na^+/Ca^{2+} solution I and II samples have force of friction smaller than this maximum force $F = 6.2 \times 10^{-8}$ N. These calculations show that the microrobots need to be made soft enough in order to pass through narrow openings.

Bacterial flagellar filaments with low modulus can change shape in the presence of flow [54], indicating a promising polymorphic transformation when swimming in various liquids. Here we report the soft microrobot can adaptively deform when swimming in viscosity liquids. As schematically shown in Fig. 4a, we observed that undering an rotating magnetic field, a soft microrobot with an original R_0 placed the soft micromotor tended to elongate slightly in the motion direction during the cockscrew motion, and tightening along the radius direction. The extracted experimental frame of soft microrobot in serial viscosity fluids were shown in Fig. S12 and Video S7 in Supporting Information. During the motion, the radius of the microrobot was observed to reduce down to certain length R_1 when reaching a relative stable status, and the radius of the samples in serial viscosity fluids were shown in Fig. 4b. Dependence of microrobot velocity on liquid viscosity and rotation frequency was shown in Fig. 4c and d. It's obvious that the increase of viscosity decreased the speed of the soft mcirorobots and the step-out frequency, the soft microrobot reached the step-out frequency at 27, 23, 21, 13, and 5 Hz, respectively, as shown in Fig. S13. After the step-out frequency, especially in higher viscosity fluids groups, the speed drop slowly and remained relatively high compared with the previously reported rigid ones whose velocity drop significantly after the step-out frequency [63], similar to what reported by Wang et al. [29]. We hypothesize that due to the hydrodynamic interactions, the soft microrobot would deform to a lower resistance morphology. Unlike rigid microrobots, the coupling between magnetic torque, body elasticity, and hydrodynamic interactions together determine the deformation and locomotion of soft microrobots. The simulation of soft microrobots swimming in serial viscosity was further performed using finite element method to better understand the hydrodynamic induced deformation (see detail in Fig. S14 in Supporting Information). It's calculated that radius decreased further with increased liquid viscosity, which is consistence with the experimental data, and both the experimental and simulated radius change results were shown in Fig. 4b.

4. Conclusion

In summary, a coaxial capillary microfluidic system combined with the dip-coating process is used to fabricate a new magnetically propelled soft microrobot, which is composed of biocompatible Ca-Alg/PEGDA hydrogel and superparamagnetic γ-Fe_2O_3 nanoparticles. The speed and direction of soft microrobots can be remotely modulated by adjusting the uniform magnetic field with a maximum speed of 3247.42 μm/s. In this work, the microrobot could navigate through constricted microchannels under programmed rotating magnetic field in various configurations, such as sinuous capillaries which resemble blood vessels, narrow openings whose cross sectional area is smaller than that of the microrobot. This deformability indicated that the magnetically propelled soft microrobots may be able to propel in complex blood vessels in bio-

logical environment. Moreover, the soft microrobots showed tightening shape change behavior during swimming, inducing increased swimming speed in fluids of high viscosity. It is worth noting that the materials used here are not limited to soft materials such as Ca-Alg/PEGDA hydrogel, and stimuli-responsive materials can also be used. While soft materials have the advantage of controllable modulus, stimuli-responsive materials allow the microrobot to actively deform into desired shapes and accomplish more complex tasks, *e.g.*, controlled drug delivery [64–66]. Hence, this new magnetically propelled soft microrobot will open new possibilities for a wide range of biomedical applications.

Declaration of Competing Interest

The authors declare that they have no known competing financial interests or personal relationships that could have appeared to influence the work reported in this paper.

Acknowledgments

This work is supported by the National Natural Science Foundation of China (51961145108, 52175009), Science and Technology Commission of Shanghai Municipality (17JC1401700, 19JC1415500), the Program of Shanghai Academic Research Leader (19XD1400600), the Shanghai Sailing Program (21YF1401600), the Fundamental Research Funds for the Central Universities and Interdisciplinary Research Foundation of HIT.

Supplementary materials

Supplementary material associated with this article can be found, in the online version, at doi:10.1016/j.apmt.2021.101237.

References

[1] J. Li, B. Esteban-Fernández de Ávila, W. Gao, L. Zhang, J. Wang, Micro/nanorobots for biomedicine: delivery, surgery, sensing, and detoxification, Sci. Rob. 2 (2017) eaam6431, doi:10.1126/scirobotics.aam6431.
[2] K.E. Peyer, L. Zhang, B.J. Nelson, Bio-inspired magnetic swimming microrobots for biomedical applications, Nanoscale 5 (2013) 1259–1272, doi:10.1039/C2NR32554C.
[3] Y.F. Mei, A.A. Solovev, S. Sanchez, O.G. Schmidt, Rolled-up nanotech on polymers: from basic perception to self-propelled catalytic microengines, Chem. Soc. Rev. 40 (2011) 2109–2119, doi:10.1039/C0CS00078G.
[4] H. Wang, M. Pumera, Fabrication of micro/nanoscale motors, Chem. Rev. 115 (2015) 8704–8735, doi:10.1021/acs.chemrev.5b00047.
[5] T.E. Mallouk, A. Sen, Powering nanorobots, Sci. Am. 300 (2009) 72–77, doi:10.1038/scientificamerican0509-72.
[6] H. Noguchi, G. Gompper, Shape transitions of fluid vesicles and red blood cells in capillary flows, Proc. Natl. Acad. Sci. USA 102 (2005) 14159, doi:10.1073/pnas.0504243102.
[7] X. Ma, A.C. Hortelao, A. Miguel-López, S. Sánchez, Bubble-free propulsion of ultrasmall tubular nanojets powered by biocatalytic reactions, J. Am. Chem. Soc. 138 (2016) 13782–13785, doi:10.1021/jacs.6b06857.
[8] Y. Tu, F. Peng, X. Sui, Y. Men, P.B. White, J.C.M. van Hest, D.A. Wilson, Self-propelled supramolecular nanomotors with temperature-responsive speed regulation, Nat. Chem. 9 (2017) 480–486, doi:10.1038/nchem.2674.
[9] G. Loget, A. Kuhn, Electric field-induced chemical locomotion of conducting objects, Nat. Commun. 2 (2011), doi:10.1038/ncomms1550.
[10] S.T. Chang, V.N. Paunov, D.N. Petsev, O.D. Velev, Remotely powered self-propelling particles and micropumps based on miniature diodes, Nat. Mater. 6 (2007) 235–240, doi:10.1038/nmat1843.
[11] B. Dong, T. Zhou, H. Zhang, C.Y. Li, Directed self-assembly of nanoparticles for nanomotors, ACS Nano 7 (2013) 5192–5198, doi:10.1021/nn400925q.
[12] B. Jurado-Sanchez, S. Sattayasamitsathit, W. Gao, L. Santos, Y. Fedorak, V.V. Singh, J. Orozco, M. Galarnyk, J. Wang, Self-propelled activated carbon Janus micromotors for efficient water purification, Small 11 (2015) 499–506, doi:10.1002/smll.201402215.
[13] D.L. Fan, Z.Z. Yin, R. Cheong, F.Q. Zhu, R.C. Cammarata, C.L. Chien, A. Levchenko, Subcellular-resolution delivery of a cytokine through precisely manipulated nanowires, Nat. Nanotechnol. 5 (2010) 545–551, doi:10.1038/nnano.2010.104.
[14] Z.H. Lin, T.Y. Si, Z.G. Wu, C.Y. Gao, X.K. Lin, Q. He, Light-activated active colloid ribbons, Angew. Chem. Int. Ed. 56 (2017) 13517–13520, doi:10.1002/ange.201708155.
[15] F.Z. Mou, J.H. Zhang, Z. Wu, S.N. Du, Z.X. Zhang, L.L. Xu, J.G. Guan, Phototactic flocking of photochemical micromotors, iScience 19 (2019) 415–424, doi:10.1016/j.isci.2019.07.050.
[16] B.H. Dai, J.Z. Wang, Z. Xiong, X.J. Zhan, W. Dai, C.C. Li, S.P. Feng, J.Y. Tang, Programmable artificial phototactic microswimmer, Nat. Nanotechnol. 11 (2016) 1087–1092, doi:10.1038/nnano.2016.187.
[17] R.F. Dong, Y. Hu, Y.F. Wu, W. Gao, B.Y. Ren, Q.L. Wang, Y.P. Cai, Visible-light-driven BiOl-based Janus micromotor in pure water, J. Am. Chem. Soc. 139 (2017) 1722–1725, doi:10.1021/jacs.6b09863.
[18] S. Palagi, A.G. Mark, S.Y. Reigh, K. Melde, T. Qiu, H. Zeng, C. Parmeggiani, D. Martella, A. Sanchez-Castillo, N. Kapernaum, F. Giesselmann, D.S. Wiersma, E. Lauga, P. Fischer, Structured light enables biomimetic swimming and versatile locomotion of photoresponsive soft microrobots, Nat. Mater. 15 (2016) 647–653, doi:10.1038/nmat4569.
[19] W. Wang, L.A. Castro, M. Hoyos, T.E. Mallouk, Autonomous motion of metallic microrods propelled by ultrasound, ACS Nano 6 (2012) 6122–6132, doi:10.1021/nn301312z.
[20] X.Y. Ding, S.C.S. Lin, B. Kiraly, H.J. Yue, S.X. Li, I.K. Chiang, J.J. Shi, S.J. Benkovic, T.J. Huang, On-chip manipulation of single microparticles, cells, and organisms using surface acoustic waves, Proc. Natl. Acad. Sci. USA 109 (2012) 11105–11109, doi:10.1073/pnas.1209288109.
[21] Z.G. Wu, T.L. Li, J.X. Li, W. Gao, T.L. Xu, C. Christianson, W.W. Gao, M. Galarnyk, Q. He, L.F. Zhang, J. Wang, Turning erythrocytes into functional micromotors, ACS Nano 8 (2014) 12041–12048, doi:10.1021/nn506200x.
[22] T.L. Xu, F. Soto, W. Gao, R. Dong, V. Garcia-Gradilla, E. Magana, X.J. Zhang, J. Wang, Reversible swarming and separation of self-propelled chemically powered nanomotors under acoustic fields, J. Am. Chem. Soc. 137 (2015) 2163–2166, doi:10.1021/ja511012v.
[23] T. Qiu, T.C. Lee, A.G. Mark, K.I. Morozov, R. Munster, O. Mierka, S. Turek, A.M. Leshansky, P. Fischer, Swimming by reciprocal motion at low Reynolds number, Nat. Commun. 5 (2014) 5119, doi:10.1038/ncomms6119.
[24] S. Tottori, L. Zhang, F.M. Qiu, K.K. Krawczyk, A. Franco-Obregon, B.J. Nelson, Magnetic helical micromachines: fabrication, controlled swimming, and cargo transport, Adv. Mater. 24 (2012) 811–816, doi:10.1002/adma.201103818.
[25] Z.G. Wu, J. Troll, H.H. Jeong, Q. Wei, M. Stang, F. Ziemssen, Z.G. Wang, M.D. Dong, S. Schnichels, T. Qiu, P. Fischer, A swarm of slippery micropropellers penetrates the vitreous body of the eye, Sci. Adv. 4 (2018), doi:10.1126/sciadv.aat4388.
[26] H. Xie, M.M. Sun, X.J. Fan, Z.H. Lin, W.N. Chen, L. Wang, L.X. Dong, Q. He, Reconfigurable magnetic microrobot swarm: multimode transformation, locomotion, and manipulation, Sci. Rob. 4 (2019), doi:10.1126/scirobotics.aav8006.
[27] A. Ghosh, P. Fischer, Controlled propulsion of artificial magnetic nanostructured propellers, Nano Lett. 9 (2009) 2243–2245, doi:10.1021/nl900186w.
[28] T.L. Li, A.N. Zhang, G.B. Shao, M.S. Wei, B. Guo, G.Y. Zhang, L.Q. Li, W. Wang, Janus microdimer surface walkers propelled by oscillating magnetic fields, Adv. Funct. Mater. 28 (2018) 1706066, doi:10.1002/adfm.201706066.
[29] X.P. Wang, X.H. Qin, C.Z. Hu, A. Terzopoulou, X.Z. Chen, T.Y. Huang, K. Maniura-Weber, S. Pane, B.J. Nelson, 3D printed enzymatically biodegradable soft helical microswimmers, Adv. Funct. Mater. 28 (2018) 1804107, doi:10.1002/adfm.201804107.
[30] R.F. Dong, J.X. Li, I. Rozen, B. Ezhilan, T.L. Xu, C. Christianson, W. Gao, D. Saintillan, B.Y. Ren, J. Wang, Vapor-driven propulsion of catalytic micromotors, Sci. Rep. 5 (2015) 13226, doi:10.1038/srep13226.
[31] X. Ma, X. Wang, K. Hahn, S. Sanchez, Motion control of urea-powered biocompatible hollow microcapsules, ACS Nano 10 (2016) 3597–3605, doi:10.1021/acsnano.5b08067.
[32] J. Li, W. Liu, T. Li, I. Rozen, J. Zhao, B. Bahari, B. Kante, J. Wang, Swimming microrobot optical nanoscopy, Nano Lett. 16 (2016) 6604–6609, doi:10.1021/acs.nanolett.6b03303.
[33] W. Gao, X. Feng, A. Pei, Y. Gu, J. Li, J. Wang, Seawater-driven magnesium based Janus micromotors for environmental remediation, Nanoscale 5 (2013) 4696–4700, doi:10.1039/C3NR01458D.
[34] X.C. Chang, C.R. Chen, J.X. Li, X.L. Lu, Y.Y. Liang, D.K. Zhou, H.C. Wang, G.Y. Zhang, T.L. Li, J. Wang, L.Q. Li, Motile micropump based on synthetic micromotors for dynamic micropatterning, ACS Appl. Mater. Interfaces 11 (2019) 28507–28514, doi:10.1021/acsami.9b08159.
[35] B. Xu, X. Lin, Y. Mei, Versatile rolling origami to fabricate functional and smart materials, Cell Rep. Phys. Sci. 1 (2020) 100244, doi:10.1016/j.xcrp.2020.100244.
[36] J.X. Li, W. Gao, R.F. Dong, A. Pei, S. Sattayasamitsathit, J. Wang, Nanomotor lithography, Nat. Commun. 5 (2014) 5026, doi:10.1038/ncomms6026.
[37] K. Melde, E. Choi, Z.G. Wu, S. Palagi, T. Qiu, P. Fischer, Acoustic fabrication via the assembly and fusion of particles, Adv. Mater. 30 (2018) 1704507, doi:10.1002/adma.201704507.
[38] A. Servant, F. Qiu, M. Mazza, K. Kostarelos, B.J. Nelson, Controlled *in vivo* swimming of a swarm of bacteria-like microrobotic flagella, Adv. Mater. 27 (2015) 2981–2988, doi:10.1002/adma.201404444.
[39] Z.G. Wu, L. Li, Y.R. Yang, P. Hu, Y. Li, S.Y.O. Yang, L.V. Wang, W. Gao, A microrobotic system guided by photoacoustic computed tomography for targeted navigation in intestines *in vivo*, Sci. Rob. 4 (2019) eaax0613, doi:10.1126/scirobotics.aax0613.
[40] J.X. Shao, M.J. Xuan, L.R. Dai, T.Y. Si, J.B. Li, Q. He, Near-infrared-activated nanocalorifiers in microcapsules: vapor bubble generation for *in vivo* enhanced cancer therapy, Angew. Chem. Int. Ed. 54 (2015) 12782–12787, doi:10.1002/anie.201506115.
[41] H.W. Huang, F.E. Uslu, P. Katsamba, E. Lauga, M.S. Sakar, B.J. Nelson, Adaptive locomotion of artificial microswimmers, Sci. Adv. 5 (2019) eaau1532, doi:10.1126/sciadv.aau1532.
[42] J.R. Baylis, J.H. Yeon, M.H. Thomson, A. Kazerooni, X. Wang, A.E. St. John, E.B. Lim, D. Chien, A. Lee, J.Q. Zhang, J.M. Piret, L.S. Machan, T.F. Burke,

N.J. White, C.J. Kastrup, Self-propelled particles that transport cargo through flowing blood and halt hemorrhage, Sci. Adv. 1 (2015) e1500379, doi:10.1126/sciadv.1500379.
[43] N. Hu, L. Wang, W. Zhai, M. Sun, H. Xie, Z. Wu, Q. He, Magnetically actuated rolling of star-shaped hydrogel microswimmer, Macromol. Chem. Phys. 219 (2018) 1700540, doi:10.1002/macp.201700540.
[44] R.A. McBath, D.A. Shipp, Swelling and degradation of hydrogels synthesized with degradable poly(β-amino ester) crosslinkers, Polym. Chem. 1 (2010) 860–865, doi:10.1039/C0PY00074D.
[45] K. Knop, R. Hoogenboom, D. Fischer, U.S. Schubert, Poly(ethylene glycol) in drug delivery: pros and cons as well as potential alternatives, Angew. Chem. Int. Ed. 49 (2010) 6288–6308, doi:10.1002/anie.200902672.
[46] G. Hwang, A.J. Paula, E.E. Hunter, Y. Liu, A. Babeer, B. Karabucak, K. Stebe, V. Kumar, E. Steager, H. Koo, Sci. Robot. 4 (2019) eaaw2388, doi:10.1126/scirobotics.aaw2388.
[47] Y. Yu, L. Shang, W. Gao, Z. Zhao, H. Wang, Y. Zhao, Microfluidic lithography of bioinspired helical micromotors, Angew. Chem. Int. Ed. 56 (2017) 12127–12131, doi:10.1002/anie.201705667.
[48] T. Li, J. Li, H. Zhang, X. Chang, W. Song, Y. Hu, G. Shao, E. Sandraz, G. Zhang, L. Li, J. Wang, Magnetically propelled fish-like nanoswimmers, Small 12 (2016) 6098–6105, doi:10.1002/smll.201601846.
[49] T. Li, J. Li, K.I. Morozov, Z. Wu, T. Xu, I. Rozen, A.M. Leshansky, L. Li, J. Wang, Highly efficient freestyle magnetic nanoswimmer, Nano Lett. 17 (2017) 5092–5098, doi:10.1021/acs.nanolett.7b02383.
[50] P. Kinnunen, B.H. McNaughton, J. Niinimäki, Note: a portable magnetic field for powering nanomotors, microswimmers, and sensors, Rev. Sci. Instrum. 84 (2013) 086109, doi:10.1063/1.4817630.
[51] K.I. Jang, H.U. Chung, S. Xu, C.H. Lee, H.W. Luan, J. Jeong, H.Y. Cheng, G.T. Kim, S.Y. Han, J.W. Lee, J. Kim, M. Cho, F.X. Miao, Y.Y. Yang, H.N. Jung, M. Flavin, H. Liu, G.W. Kong, K.J. Yu, S.I. Rhee, J. Chung, B. Kim, J.W. Kwak, M.H. Yun, J.Y. Kim, Y.M. Song, U. Paik, Y.H. Zhang, Y. Huang, J.A. Rogers, Soft network composite materials with deterministic and bio-inspired designs, Nat. Commun. 6 (2015) 6566, doi:10.1038/ncomms7566.
[52] S. Utech, A.R. Boccaccini, A review of hydrogel-based composites for biomedical applications: enhancement of hydrogel properties by addition of rigid inorganic fillers, J. Mater. Sci. 51 (2016) 271–310, doi:10.1007/s10853-015-9382-5.
[53] K. Son, F. Menolascina, R. Stocker, Speed-dependent chemotactic precision in marine bacteria, Proc. Natl. Acad. Sci. USA 113 (2016) 8624–8629, doi:10.1073/pnas.1602307113.
[54] H. Hoshikawa, R. Kamiya, Elastic properties of bacterial flagellar filaments: II. Determination of the modulus of rigidity, Biophys. Chem. 22 (1985) 159–166, doi:10.1016/0301-4622(85)80038-7.
[55] D. Park, D. y. Yoon, J.C. Kim, Monoolein cubic phase including *in situ* ionically gelled alginate and its salt-responsive release property, J. Dispers. Sci. Technol. 39 (2018) 18–25, doi:10.1080/01932691.2017.1289848.
[56] B. ten Hagen, F. Kümmel, R. Wittkowski, D. Takagi, H. Löwen, C. Bechinger, Gravitaxis of asymmetric self-propelled colloidal particles, Nat. Commun. 5 (2014) 4829, doi:10.1038/ncomms5829.
[57] S. Tottori, L. Zhang, F. Qiu, K.K. Krawczyk, A. Franco-Obregón, B.J. Nelson, Magnetic helical micromachines: fabrication, controlled swimming, and cargo transport, Adv. Mater. 24 (2012) 811–816, doi:10.1002/adma.201103818.
[58] A. Sanchez, V. Magdanz, O.G. Schmidt, S. Misra, Magnetic control of self-propelled microjets under ultrasound image guidance, in: Proceedings of the IEEE RAS & EMBS International Conference on Biomedical Robotics and Biomechatronics (BioRob), 2014, pp. 169–174.
[59] D. Vilela, U. Cossío, J. Parmar, A.M. Martínez-Villacorta, V. Gómez-Vallejo, J. Llop, S. Sánchez, Medical imaging for the tracking of micromotors, ACS Nano 12 (2018) 1220–1227, doi:10.1021/acsnano.7b07220.
[60] X. Yan, Q. Zhou, M. Vincent, Y. Deng, J. Yu, J. Xu, T. Xu, T. Tang, L. Bian, Y.X.J. Wang, K. Kostarelos, L. Zhang, Multifunctional biohybrid magnetite microrobots for imaging-guided therapy, Sci. Robot. 2 (2017) eaaq1155, doi:10.1126/scirobotics.aaq1155.
[61] M. Rong, H. Liu, M. Scaraggi, Y. Bai, L. Bao, S. Ma, Z. Ma, M. Cai, D. Dini, F. Zhou, High lubricity meets load capacity: cartilage mimicking bilayer structure by brushing up stiff hydrogels from subsurface, Adv. Funct. Mater. 30 (2020) 2004062, doi:10.1002/adfm.202004062.
[62] J. Lighthill, Flagellar hydrodynamics, SIAM Rev. 18 (1976) 161–230, doi:10.1137/1018040.
[63] L. Zhang, J.J. Abbott, L. Dong, K.E. Peyer, B.E. Kratochvil, H. Zhang, C. Bergeles, B.J. Nelson, Characterizing the swimming properties of artificial bacterial flagella, Nano Lett. 9 (2009) 3663–3667, doi:10.1021/nl901869j.
[64] J. Cui, T. Huang, Z. Luo, P. Testa, H. Gu, X. Chen, B.J. Nelson, L.J. Heyderman, Nanomagnetic encoding of shape-morphing micromachines, Nature 575 (2019) 164–168, doi:10.1038/s41586-019-1713-2.
[65] Y. Zhao, C. Lo, L. Ruan, C. Pi, C. Kim, Y. Alsald, I. Frenkel, R. Rico, T. Tsao, X. He, Somatosensory actuator based on stretchable conductive photothermally responsive hydrogel, Sci. Robot. 2021, 6, eabd5483, doi:10.1126/scirobotics.abd5483.
[66] S.R. Sirsi, M.A. Borden, State-of-the-art materials for ultrasound-triggered drug delivery, Adv. Drug Deliv. Rev. 72 (2014) 3–14, doi:10.1016/j.addr.2013.12.010.